ELSEVIER Solar Energy Materials and Solar Cells 41/42 (1996) 381–393

Solar Energy Materials and Solar Cells

Micro through nanostructure investigations of polycrystalline CdTe: Correlations with processing and electronic structures

D.H. Levi [a], H.R. Moutinho [a], F.S. Hasoon [a], B.M. Keyes [a], R.K. Ahrenkiel [a], M. Al-Jassim [a], L.L. Kazmerski [a], R.W. Birkmire [b]

[a] *National Renewable Energy Laboratory, 1617 Cole Blvd., Golden, CO 80401, USA*
[b] *Institute of Energy Conversion, University of Delaware, Newark, DW 19716, USA*

Abstract

This paper provides first-time correlations of the nanoscale physical structure with the macroscale electronic and optical properties of CdTe/CdS thin films for several standard deposition techniques. Atomic force microscopy (AFM) was used to determine the micro and nanostructures of polycrystalline CdTe thin films used in photovoltaic (PV) cell fabrication. Photoluminescence (PL) was used to determine band gap, relative defect density, and photoexcited carrier lifetime. Cross-sectional scanning tunneling microscopy (STM) was used to determine the nanoscale electronic properties. Nanostructural features (nanograins), beyond the spatial resolution of conventional scanning electron microscopy (SEM), were observed and characterized in as-deposited CdTe. The correlations of the proximal probe measurements of the physical and electronic structure with the optically determined electronic properties were used to show the effects of the chemical and heat processing, directly and conclusively. A particularly striking effect with important implications for PV applications is the diffusion of sulfur across the CdTe/CdS interface during heat treatment.

1. Introduction

Research-quality CdTe thin-film solar cells have demonstrated efficiencies up to 15.8% [1]. Improvements above the 10% efficiency regime have largely been accomplished through a combination of a better understanding of materials properties and chemistry, related advancements in device/materials processing [2], and interface engineering. The active layer of this solar cell is subjected to various post-deposition processing, including chemical and thermal treatments, and these lead to improvements in the electro-optical properties of the semiconductors. Morphology, inter grain properties, and grain configurations are very important,

0927-0248/96/$15.00
SSDI 0927-0248(95)00110-7

not only for optimal electro-optical characteristics of the films for PV applications, but also for junction formation and electrical contacting.

In this paper, the morphology of polycrystalline CdTe films is evaluated using AFM, and correlated with conventional SEM images. The first direct observations and measurements of nanoscale structures in these PV semiconductors are reported as functions of the thermal and chemical processing. These are, in turn, correlated with the electronic structure as determined through photoluminescence spectroscopy, photoexcited carrier lifetime, and cross-sectional scanning tunneling microscopy (STM). Indications for improved cell behavior due to the thermal and chemical processing are reported for the first time based upon the correlations of nanoscale imaging with optical characterization.

2. Micro and nanostructural properties

Until recently, the scanning electron microscope has served as the major analytical tool for investigating morphology and physical properties, but it has several limitations. First, it is limited in resolution to the 2–5 nm region. Second, if the films are not conductive (typical for device-quality CdTe), charging effects associated with the high-energy electron beam impair or negate the imaging and/or resolution. Atomic force microscopy (AFM) overcomes these limitations, and can be utilized to provide previously unattainable information on the topography and electronic structure of these materials. Spatial resolutions in the nanometer and atomic ranges can be attained, as well as the advantages of digital imaging (for the exact determinations of surface features, quantitative evaluations of roughness, and image analysis from different perspectives).

3. Experimental

Polycrystalline CdTe thin films were deposited on CdS or conducting oxide substrates (SnO_2 or ITO) using physical vapor deposition (PVD), closed-space vapor sublimation (CSS), and radio-frequency sputtering (RFS). The CSS deposited samples were approximately 4.5 μm thick while the PVD and RFS samples were in the 2–3 μm range. Post-deposition heat treatments were carried out by depositing a thin layer of $CdCl_2$ from a $CdCl_2$-saturated methanol solution. The samples were then heat treated for 30 minutes at 300°, 350°, or 400°C in a tube furnace. Solar cells made from samples treated at 400°C had total area efficiencies of 8 to 9% for the RFS and PVD samples and 11% for the CSS samples.

AFM measurements were performed using an AFM Autoprobe LS from Park Scientific Instruments, with Si_3N_4 and Si cantilevers. The Autoprobe LS uses a cantilever with an attached tip as the analytical probe [3]. Voltages are transformed to distance by calibration of the piezoelectrics. The movements are calibrated using standards (e.g., graphite (HOPG) or gratings). Image dimensions may range from many microns to several angstroms.

4. Results and discussion

Investigations of the surface morphology of CdTe thin films have typically reported grain dimensions ranging from 1000Å to microns evaluated by conventional SEM [4–6]. However, the enhanced resolution of the proximal probe techniques indicates that as-deposited films sometimes have two feature regimes: features with diameters in the SEM-determined ranges, and subgrains within these larger features, with diameters of hundreds of angstroms. Fig. 1a and Fig. 1b show a comparison of the surface of an RFS CdTe on SnO_2 film, imaged by SEM and AFM, respectively. Both micro graphs show identical surface structures in this resolution range, with grain sizes in the 0.1–0.3 μm range. Fig. 2 shows an AFM image of the same film under higher magnification conditions—beyond those capable with the SEM. Much smaller grains, with 200–400Å cross sections, are resolved. The existence and nanostructure of this double grain structure depend upon the deposition method, the structure of the surface (substrate or sub layer) on which the film is grown, and on post-deposition processing. The thermal and chemical processing steps that are critical in producing higher efficiency CdTe thin-film devices have mixed correlations with changes in the films' physical properties. We have conducted a comprehensive AFM study of the micro- and nano-structure of CdTe thin films as a function of deposition technique, substrate structure, and processing conditions. An illustration of the changes in microstructure with processing is provided by Figs. 2 and 3. The as-deposited film is shown in Fig. 2, with 200–400Å nanoscale grains. Fig. 3 shows the same film following heat-treatment with $CdCl_2$ at 400°C for 30 minutes. It is clear from the AFM image in Fig. 3 that the $CdCl_2$ heat treatment produces a completely recrystallized nanostructure, with elimination of the nanoscale subgrains.

The AFM images illustrate the dramatic evolution of the structure of sputtered CdTe films deposited on SnO_2. We have studied the evolution of the structure of CdTe films under five different deposition conditions and three post-growth processing conditions. These results are summarized in Table 1. The RFS-CdTe films deposited on SnO_2 are the only samples that show the double grain structure as illustrated in Fig. 2. Films sputter-deposited on CdS/ITO substrates show only very small grains (700Å) without the larger grain structure. The PVD-deposited films have an average initial grain size of 3000Å, independent of substrate. CSS-deposited films show a relatively large initial grain size of 1.5 μm. We have studied the changes in microstructure using the standard $CdCl_2$ heat treatment at 300°, 350°, and 400°C. Grain sizes for PVD and RFS films show little change at 300° or 350° but heat treatment at 400°C produces significant grain growth. The CSS films started with the largest grain sizes, and showed little change in their microstructure for any processing temperature.

5. Optoelectronic properties

We have correlated our nanostructural investigations of these films with their electronic properties using optical methods. Photoluminescence (PL) spectroscopy

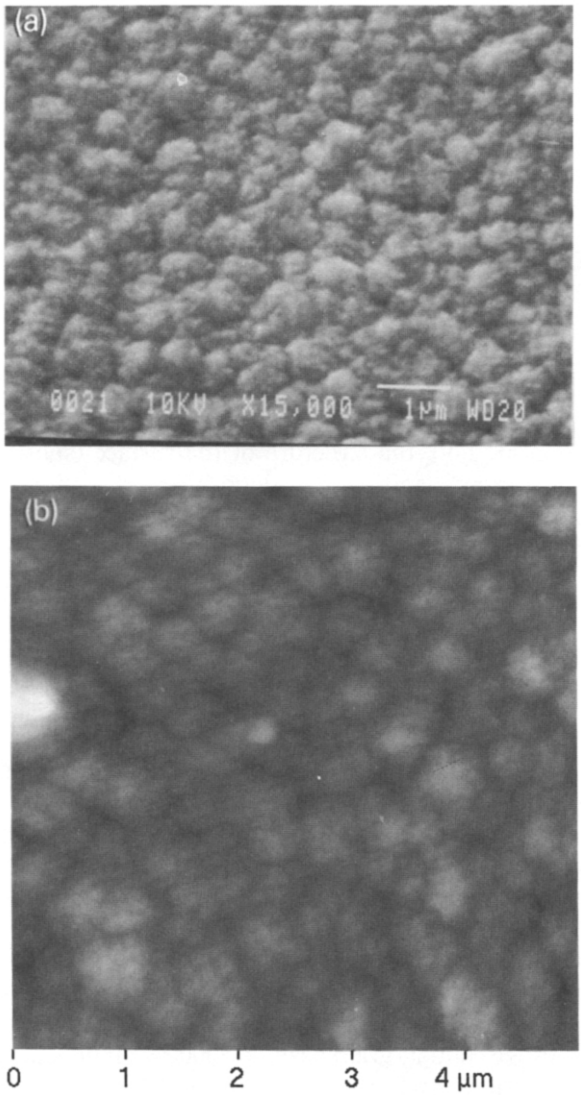

Fig. 1. (a) SEM image of a sputter grown $CdTe/SnO_2$ film. (b) AFM image of the same $CdTe/SnO_2$ film as shown in Fig. 1a.

and time-resolved photoluminescence (TRPL) have been used to evaluate the electronic structure and relative defect densities in these films as a function of deposition technique and processing. All of the films follow the general trend of improved PL efficiency and lifetime with processing. Differences in how the films respond to the standard chemical and heat treatments provide clues to the nature of the electronic and structural changes that are key to producing high efficiency CdTe/CdS PV cells.

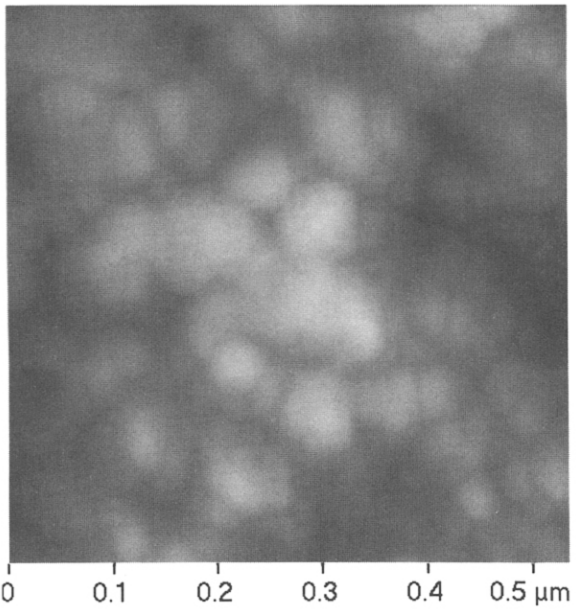

Fig. 2. High resolution AFM image of the same film as in Fig.1 showing the 200–400Å nanoscale grains within the larger grains detected at the coarser SEM resolution.

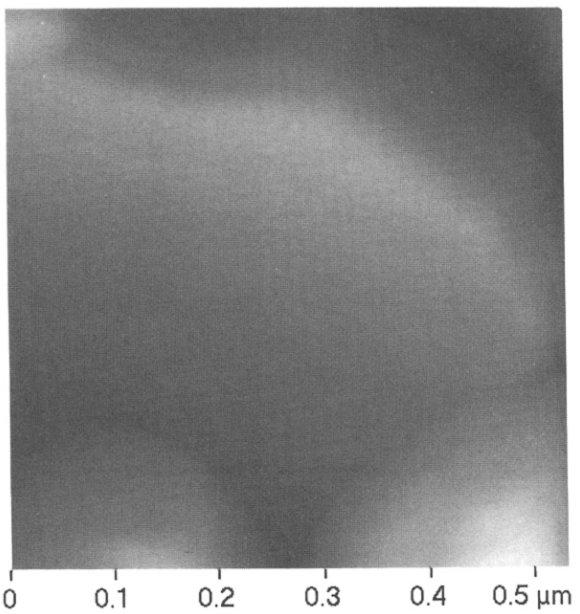

Fig. 3. High resolution AFM of RFS-CdTe/Sno_2 film following $CdCl_2$ heat treatment at 400°C showing complete coalescence of the nanograins.

6. Experimental

PL and TRPL measurements were conducted using the same experimental apparatus. Photoexcitation was provided by a mode-locked, cavity-dumped dye laser operating at repetition rates of either 1 Mhz or 38 Mhz at a wavelength of 600 nm. At room temperature, photoexcitation densities on the order of 10^{16} cm^{-3} were necessary to achieve adequate PL intensities for the measurements. Photoluminescence was collected and then dispersed in a Spex model 1672S 0.25 m subtractive double spectrometer. Single photon detection was achieved using a Hamamatsu 2809U microchannel plate photomultiplier. Time resolved measurements were performed using standard time-correlated single photon counting techniques [7]. System resolution is approximately 20 ps using deconvolution techniques. Photoexcitation and photoluminescence collection were through the glass substrate. For photoexcitation at 600 nm, CdS is transparent whereas the absorption depth in CdTe is several thousand angstroms. Hence, carriers are excited only in the CdTe absorber near the CdTe/CdS junction. Because of this the PL and TRPL measurements are sensitive to the material near the CdTe/CdS junction, in contrast to the AFM measurements, which probe the material at the top of the CdTe layer.

7. Results and discussion

Photoluminescence lifetime and radiative efficiency are two optical properties that are quite sensitive to the concentration and type of defects present. Because defects are concentrated at the grain boundaries these parameters should also be quite sensitive to grain size. Fig. 4 presents the relative radiative efficiency of the five types of samples as a function of processing conditions. In this context relative radiative efficiency is defined as the PL intensity at the peak of the PL spectrum under identical excitation conditions for each sample. It is clear that the radiative efficiency for as-grown and 300°C treated samples is virtually nil. This indicates a high concentration of defects which act as fast, non-radiative recombination

Table 1
CdTe grain sizes versus processing for various growth techniques and substrates

Growth method	Substrate structure	Grain Size (μm)				Plot symbol
		As received	$CdCl_2$ 300°C	$CdCl_2$ 350°C	$CdCl_2$ 400°C	
CSS	CdTe/CdS/ITO/Glass	1.5	1.5	1.5	1.5	■
PVD	CdTe/ITO/Glass	0.3	0.3	0.4	1.5	◆
PVD	CdTe/CdS/ITO/Glass	0.3	0.4	0.4	1.5	·
RFS	CdTe/SnO_2/Glass	0.4	0.4	0.5	0.5–0.8	▼
	"	0.04	0.04	0.04		
RFS	CdTe/CdS/ITO/Glass	0.07	0.04	0.07	0.2–0.7	▲

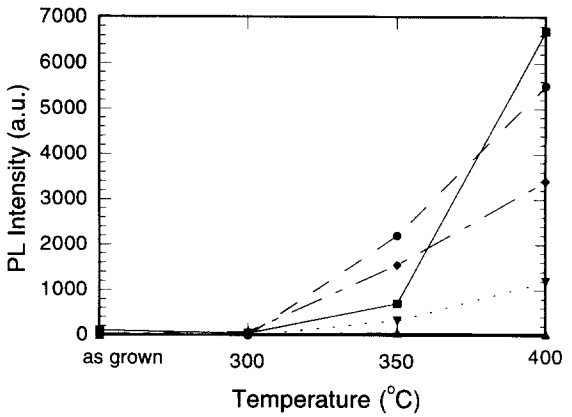

Fig. 4. Room temperature photoluminescence intensities versus processing conditions for each of the five types of samples: (■) CSS-CdTe/CdS, (♦) PVD-CdTe/ITO, (·) PVD-CdTe/CdS, (▲) RFS-CdTe/CdS, (▼) RFS-CDTe/SnO.

centers. Typically such defects are deep levels near mid-gap which serve as centers for Shockley–Reed–Hall (SRH) recombination. With the exception of the RFS-CdTe/CdS, all samples treated at 350°C show a significant increase in radiative efficiency, with a much larger increase for the samples treated at 400°. We believe the anomalous behavior of the RFS CdTe/CdS samples is due to structural damage occurring during heat treatment, which is described in another publication [8]. The relation between radiative efficiency and grain size for the PVD samples and the RFS samples is qualitatively as one would expect. It has been shown that if bulk and surface recombination rates remain unchanged with processing, there should exist a direct linear relation between PL efficiency and grain size [9]. Our results show that PL efficiency increases much more rapidly than grain size. This indicates that the $CdCl_2$ heat treatment not only promotes grain growth, but also passivates defects. This conclusion is reinforced by the results for the CSS samples where there is virtually no change in grain size, yet a large increase in radiative efficiency. The dramatic increase in radiative efficiency seen in the 400°C treated CSS film indicates that the $CdCl_2$ heat treatment is a very effective agent for passivation of the defects responsible for fast non-radiative recombination.

Under the excitation conditions used in these experiments, photoluminescence decays in polycrystalline CdTe films typically show a two-component decay. Based on measurements at differing excitation densities and temperatures we infer that the early, fast component is produced by radiative and non-radiative recombination, and carrier trapping in shallow defect levels. Due to uncertainty in doping levels it is unclear whether the radiative component of the decay is a high or low injection lifetime. The late, slow component is affected by all three of the former factors, but is primarily governed by the rate of escape of carriers from the shallow traps. Our measurements of PL intensity versus excitation density indicate that non-radiative recombination is the dominant decay mechanism in these films.

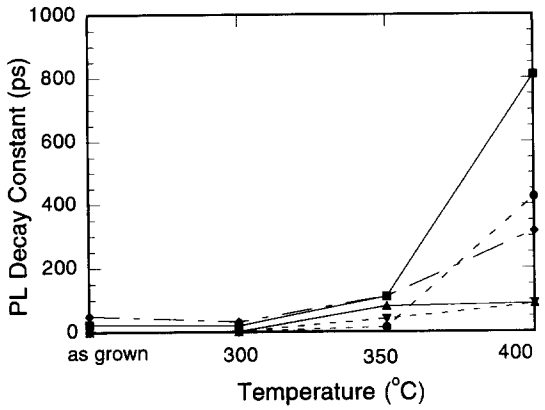

Fig. 5. Photoluminescence decay time constant at room temperature versus processing conditions for each of the five types of samples: (■) CSS-CdTe/CdS, (♦) PVD-CdTe/ITO, (·) PVD-CdTe/CdS, (▲) RFS-CdTe/CdS, (▼) RFS-CDTe/SnO.

Hence the fast PL decay component should be the clearest indicator of material quality. Fig. 5 illustrates the dependence of the fast decay component on processing for each of the five sample types. These results support our interpretation of the radiative efficiency data. PL lifetimes are quite short initially, but show dramatic improvement after the heat treatment. The percentage improvement in PL lifetimes corresponds well with improvements in PL efficiency. The final PL lifetimes and efficiencies also correspond well with relative grain sizes among the various samples. As discussed in footnote [8], we believe the RFS samples suffer structural damage during heat treatment, leading to poor optical and electronic quality.

Table 2 lists the peak PL wavelength for each sample in the processing matrix. A trend worthy of note in this data is that the as-grown samples produce PL at 820 nm, corresponding to 1.51 eV, the band gap of CdTe at room temperature. The intermediate processing temperatures produce intermediate wavelengths. The interesting result occurs for the 400°C processed samples. All of the samples deposited on CdS substrates produce PL at 845 nm, or 1.47 eV. Samples deposited

Table 2
Room temperature photoluminescence peak wavelength for each sample studied

Growth method	Film composition	PL Peak Wavelength (nm)				Plot symbol
		As deposited	$CdCl_2$ 300°C	$CdCl_2$ 350°C	$CdCl_2$ 400°C	
CSS	CdTe/CdS/ITO/Glass	820	820	828/845	845	■
PVD	CdTe/ITO/Glass	820	825/850	832/880	824	♦
PVD	CdTe/CdS/ITO/Glass	–	–	825	845	·
RFS	CdTe/CdS/ITO/Glass	–	–	840	845	▼
RFS	CdTe/SnO/Glass	–	–	820	820	▲

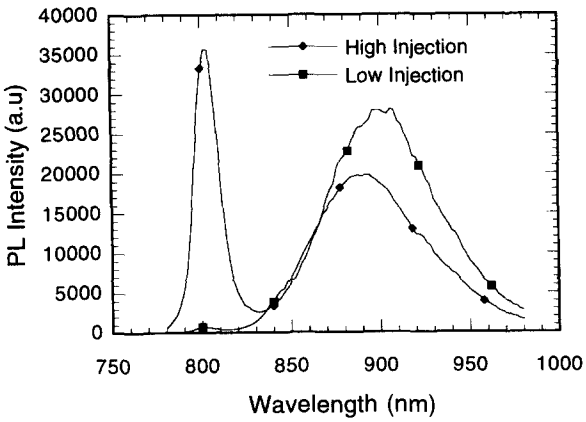

Fig. 6. Photoluminescence spectra at 77K for the 400°C $CdCl_2$-processed CSS CdTe/CdS sample. High injection corresponds to approximately 8×10^{15} cm^{-3} photoexcited carriers, while low injection is approximately 2×10^{15} cm^{-3}.

on conducting oxides still luminesce at or near the CdTe band gap – – 820 nm. To determine the origin of this shift we measured PL at 77K for the four CSS deposited samples. All of the samples produced two distinct emission bands, similar to spectra measured in MBE-grown single-crystal CdTe at 77K. These spectra are shown, for high and low photoinjection conditions, in Fig. 6 for the 400°C processed CSS sample. By comparison with earlier research on single-crystal CdTe, we have identified the higher energy emission at 1.55 eV as band-to-band photoluminescence and the broad, lower energy emission at 1.4 eV as photoluminescence associated with defects [10]. This assignment is verified by the relative intensity dependencies of the two PL emission bands. At high intensities the higher energy, band-to-band emission dominates, while at low intensities the defect emission dominates [11]. We conclude that samples deposited on CdS substrates have undergone a band gap reduction of 45 meV during the 400°C heat treatment. Data on band gap versus composition for the ternary CdTeS indicate that CdTeS with approximately 2% sulfur would have a band gap of 1.47 eV [12]. As discussed previously, our PL measurements are sensitive primarily to the material near the CdTe/CdS interface. A layer of relatively smaller band gap material near the interface would tend to absorb and subsequently re-emit PL from the bulk CdTe region at its lower bandgap. The degree of this effect is dependent on the thickness of the ternary layer, hence the band gap of the CdTeS layer may be even smaller than that indicated by the energy of the PL peak. The observed evolution of the PL maximum for samples deposited on CdS indicates diffusion of sulfur into the CdTe near the interface. This result is consistent with a previous report of sulfur/tellurium interdiffusion occurring during $CdCl_2$ heat treatment. That study utilized X-ray diffraction, optical absorption, and quantum efficiency measurements to verify changes in band gap and lattice constant [13].

8. Nanoscale electronic properties

To further corroborate our interpretation of the photoluminescence results we have used cross-sectional scanning tunneling microscopy (STM) to probe the current–voltage characteristics of the CdTe/CdS interface. Scanning probe microscopies and spectroscopies provide exceptional resolution for direct mapping of spatial variations of electronic properties, as compared to PL, C–V, or photoemission techniques. Cross-sectional STM is becoming an increasingly utilized tool to study the electronic structure of semiconductor heterojunctions [14–19]. These techniques provide information on the precise determination of band offsets, measurement of asymmetrical electronic transition widths, and detailed mapping of conduction band structures.

9. Experimental

The spectroscopic, cross-sectional STM measurements were performed using the atomic processing microscope (APM) [20]. The differential conductivity [d(ln I)//dV/V] provides a chemical representation relating to the detected electronic states. The dependence of the tunneling current, I, on the voltage is used to determine the band gap of the region under investigation.

The basic STM is of the inverted tube scanner design, with an automated tip approach. The spectroscopy is accomplished through the analysis of I–V characteristics, controlled with lateral spatial resolutions to about 1.5Å. The sample biasing incorporated potential differences between the STM probe and the exact sample surface. The CdS/CdTe structures were fractured in vacuo, and examined across the exposed junction region. Relatively flat, defect-free regions were care-

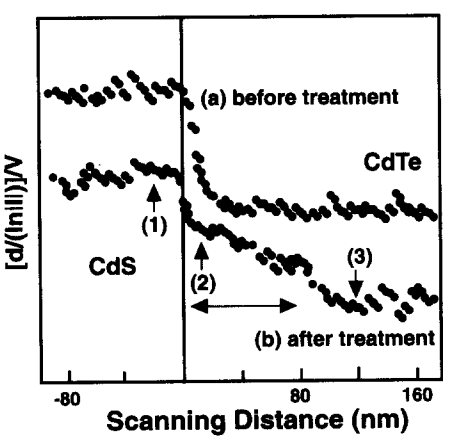

Fig. 7. STM spectroscopic conductivity scan across the CdS/CdTe junction region before and after $CdCl_2$-processing. This clearly shows a mixed Cd(Te)S phase roughly 1000Å into the CdTe side of the junction. The points labeled 1,2, and 3 specify the positions for the I–V measurements shown in Fig. 8.

fully selected to minimize artifacts from the topography and non-homogeneities such as the grain boundaries. Such effects can lead to differences in Fermi level pinning (or unpinning), and tip-induced band bending. This is especially sensitive in this case in which the CdTe and CdS have lower conductivities, and the carrier densities cannot adequately screen the field within a sufficiently short length [21]. In addition, defects (e.g., grain boundaries) have depletion regions that can interfere with the electronic state information of interest at the heterojunction. All surfaces examined in this study had nanoscale flatness, with topographical roughness less than 6 nm over the 300 nm scanning distances. Even such relative flatness contributes to scatter in the observed cross-sectional electronic data observed in Fig. 7.

10. Results and discussion

Fig. 7 shows a spectroscopic conductivity scan across the CdS/CdTe junction region. The normalized conductivity, $[\mathrm{d}(\ln|I|)/\mathrm{d}V]$ provides a *parameter-free* procedure to determine spectroscopic and electronic information [22,23]. The ratio of this to the total conductivity, I/V, provides a measure of the surface state density [24,25]. This also removes the physical (exponential) dependence of tip-sample separation. Basically, if the tunneling current has a power law dependence, $I \sim (V - V_0)^n$ near the band threshold, V_0, then $\mathrm{d}(\ln|I|)/\mathrm{d}V = n/(V - V_0)$ [26]. In the present case, the n factors were found to be consistently in the range 1.8 to 1.9 over more than 1 V of sample bias, consistent with the power law dependence. From this, the closer to the band edge or threshold, the larger is this conductivity [27]. Thus, the CdS is found to have a larger value of normalized conductivity in

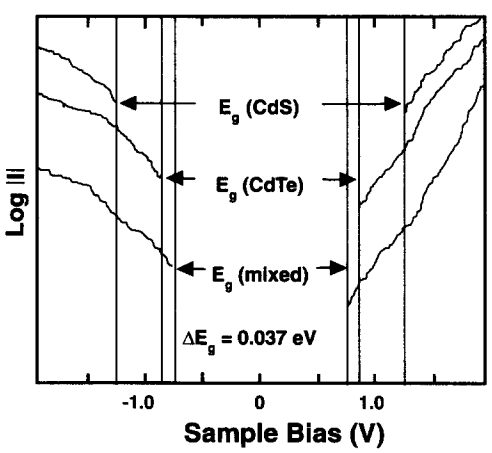

Fig. 8. Logarithmic plot of STM: tunneling current spectra, acquired at three distinct points across the CdTe/CdS junction after $CdCl_2$-processing. The bias voltage measured between current turn-off and turn-on corresponds to the material bandgap. We find a band gap reduction of 37 meV in the mixed phase region.

Fig. 7. Before treatment, the normalized conductivity, $[d(\ln|I|)/dV]/V$, shows a relatively sharp transition from the CdS side to the CdTe. In comparison, the spectroscopic data taken under identical conditions for the post-treatment sample (400°C with $CdCl_2$) indicates a much more gradual transition from CdS to CdTe, occurring over roughly 1000Å. This difference is due the change in conductivity produced by diffusion of sulfur into the CdTe region near the heterojunction.

Fig. 8 presents several tunneling current spectra, acquired at three distinct points identified in the spectroscopic data of Fig. 7. The first I–V spectrum taken in the CdTe region gives the value of the band gap of that semiconductor. Most of the important spectroscopic data is found in the tunneling I–V characteristics, but the extraction of this information is sometimes complex [23]. However, the determination of the band edge is accomplished by the careful fit of this I–V characteristic near the threshold [28]. Fig. 8 presents such tunneling current spectra showing log $|I|$ versus V, acquired at three distinct points identified in the spectroscopic data of Fig. 7. In the region between the CdS and the CdTe, a mixed phase is determined, with a bandgap reduction of 0.037 eV. These data complement those obtained by the PL studies, and support the existence of a mixed Cd(TeS) region at the heterointerface, resulting from the chemical and thermal treatment. This is the first direct nanoscale observation of this effect.

11. Conclusions

Our proximal probe measurements of this sample matrix demonstrate that the nanostructure of polycrystalline CdTe films depends on both substrate and deposition method. We have observed a unique "double-grain" structure in RFS CdTe deposited on SnO_2 substrates which eventually disappears with $CdCl_2$ heat treatment.

The correlations we have established between the nanostructure and optical properties of polycrystalline CdTe thin films show that not only does the $CdCl_2$ heat treatment enhance grain size, but also passivates defects. In the case of the CSS deposited films, the $CdCl_2$ heat treatment passivates defects without producing any change in grain size.

Finally, we have verified that sulfur diffuses across the CdTe/CdS interface during heat treatment. It appears that this mixing effect at the CdTe–CdS heterojunction produces a graded band gap in the CdTe absorber layer similar to that intentionally engineered into copper–indium–gallium–selenide thin films used for PV applications [29]. Such a graded band gap could be an important factor in the efficiency of carrier collection in CdTe/CdS PV cells.

Acknowledgements

This work partially supported under DOE contract DE-AC36-83CH10093 with NREL.

References

[1] C. Ferekides, J. Britt, Y. Ma and L. Killian, 23rd IEEE Photovoltaic Specialists Conf., 1993, p. 389.
[2] A.J. Nelson, F. Hasoon and D. Levi, J. Vac. Sci. Technol. A12(5) (1994) 2803.
[3] J. Frommer and E. Meyer, J. Phys.: Condens. Matter 3 (1991) S1.
[4] T.L. Chu, S.S. Chu, J. Britt, C. Ferekides, C. Wang, C.Q. Wu and H.S. Ullal, IEEE Electron Dev. Lett. 13 (1992) 303.
[5] S. Albright, B. Ackerman and J.F. Jordan, IEEE Trans. Electron. Dev. 37 (1990) 434.
[6] B.N. Baron, R.W. Birkmire, J.E. Phillips, W.N. Shafarman, S.S. Hegedus and B.E. McCandless, Tech. Rpt., Contract No. XL-9-19032-1, SERI, Golden, CO, 1990.
[7] R.K. Ahrenkiel, D.J. Dunlavy and T. Hanak, Solar Cells 24 (1988) 339.
[8] AFM microprobe results on the same set of samples which were reported earlier describe microscopic craters formed by apparent explosions of gas trapped below the surface in RFS materials. For more details see: H.R. Moutinho, F.S. Hasoon, F. Abulfotuh and L.L. Kazmerski Proc. 1994 AVS Symposium, in press.
[9] R.K. Ahrenkiel, B.M. Keyes, L. Wang and S.P. Albright, 22nd IEEE Photovoltaic Specialists Conf., 1991, p. 940.
[10] T.H. Myers, J.F. Schetzina, S.T. Edwards and A.F. Schreiner, J. Appl. Phys. 54(7) (1993) 4232.
[11] For a complete discussion of this effect see, e.g., J.I. Pankove, Optical Processes in Semiconductors (Dover, New York, NY, 1971) Ch. 6.
[12] R. Hill and D. Richardson, Thin Solid Films 18 (1973) 25.
[13] B.E. McCandless and Robert W. Birkmire, Solar Cells 31 (1991) 527.
[14] J.A. Dagata, Appl. Phys. Lett. 59 (1991) 3288.
[15] S. Gwo, K. J. Chao and B. Streetman, Appl. Phys. Lett. 61 (1992) 1104.
[16] R.M. Feenstra, Appl. Phys. Lett. 61 (1992) 795.
[17] T. Kato and F. Osaka, Jpn. J. Appl Phys. 30 (1991) L1586.
[18] S. Gwo, K. J. Chao, C.K. Shih, D. Sadra and B. Streetman, Phys. Rev. Lett. 71 (1993) 1883.
[19] T. Kato and F. Osaka, J. Appl. Phys. 72 (1992) 5716.
[20] L.L. Kazmerski, Jpn. J. Appl. Phys. 72 (1992) 5716.
[21] R.M. Feenstra and J.A. Stroscio, J. Vac. Sci. Technol. B5 (1987) 923.
[22] R.M. Feenstra, J.A. Stroscio, J. Tersoff and J. Fein, Phys. Rev. Lett. 58 (1987) 1192.
[23] J.A. Dagata and W. Tseng, Appl. Phys. Lett. 62 (1993) 591.
[24] N.D. Lang, Phys. Rev. B34 (1986) 594.
[25] J.A. Stroscio, R.M. Feenstra and A.P. Fein, Phys. Rev. Lett. 57 (1986) 2579.
[26] A Vaterlaus and R.M. Feenstra, J. Vac. Sci. Technol. B11 (1993) 1502.
[27] R.M. Feenstra, in: H.W.M. Salemink (Ed.), Proc. Conf. on Physical Properties of Semicond. Interfaces at Sub-Nanometer Scale (Kluwer, The Netherlands, 1994) pp. 30–39.
[28] E.T. Yu, M.B. Johnson and J.-M. Halbout, Appl. Phys. Lett. 61 (1992) 201.
[29] M. Contreras, J. Tuttle, D. Du, Y. Qu, A. Swartzlander, A. Tennant and R. Noufi, Appl. Phys. Lett. 44 (1993) 1827.